Journal of Materials Chemistry A

Accepted Manuscript

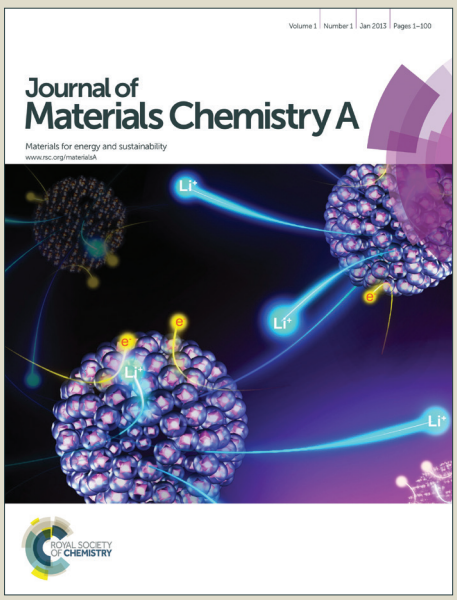

ROYAL SOCIETY OF CHEMISTRY

www.rsc.org/materialsA

Materials Chemistry A Cite this:
DOI: TA-ART-11-2013-014720

www.rsc.org/xxxxxx

PAPER

Porous $Li_2C_8H_4O_4$ coated with N-doped carbon by using CVD technology as an anode material for Li-ion batteries†

Haiquan Zhang, Qijiu Deng, Aijun Zhou, Xinquan Liu and Jingze Li*

Received (in XXX, XXX) Xth XXXXXXXXX 20XX, Accepted Xth XXXXXXXXX 20XX
DOI: 10.1039/b000000x

Lithium terephalate ($Li_2C_8H_4O_4$) and its carboxylate-based derivatives have been proposed as advanced organic anodes for low cost lithium/sodium ion batteries. One of the key barriers for practical application is poor rate capability due to the intrinsic low electronic conductivity of most organic materials at room temperature. To overcome this issue, porous microspheres consisting of $Li_2C_8H_4O_4$ nanoparticles were synthesized by a common spray drying method for the first time. Furthermore, a straight-forward surface coating technique was developed using urea powder as nitrogen and carbon sources simultaneously. Consequently, N-doped carbon layer was uniformly coated onto nanostructured $Li_2C_8H_4O_4$ electroactive material at 400 ºC by chemical vapor deposition. The composite electrode displays excellent electrochemical performance under high current rate even at room temperature.

Introduction

Rechargeable lithium ion batteries (LIBs) have been widely used in portable electronic devices due to high power density. Furthermore, LIBs have been highly appreciated as the promising energy-storage candidates for electric vehicle and stationary energy storage.[1] As a key part of LIBs, anode material including transition metal oxide[2], carbonaceous material[3], tin-based material[4] and silicon-based material[5], has been the cynosure of many eyes around the world in the past three decades. Graphite as a conventional commercial anode material displays a slow Li^+ ion diffusion at low temperature, and its quite low insertion potential may cause the risk of the battery safety.[6] As for tin-based or silicon-based materials, the huge volume change during electrochemical Li^+ ion insertion/extraction process irreparably brings about cracking of the electrode structure, which rapidly leads to the end of the cycle life.[4-5] Transition metal oxide anode generally follows conversion reaction mechanism suffering from lower columbic efficiency in the initial cycles.[2]

As an alternative to inorganic anode matters prepared from limited mineral resources, organic electrode materials have the advantages of low cost due to abundant storage on the earth, low molecular weight, high specific capacity, and environmental friendless.[7] In general, these organic electrode materials can be divided into four types including organic carbonyl compounds, organosulfur compounds, organic free radical compounds, and conducting polymers.[7-8] Carbonyl compounds were the earliest organic electrode materials investigated from 1960's.[7] Recently, it is found that metal salt of the carbonyl molecules can abruptly improve the cycling stability by depressing the solubility of the electroactive material in aprotic organic electrolyte. Lithium terephthalate ($Li_2C_8H_4O_4$, PTAL), a carboxylate-based organic anode material, keeps 78% of its theoretical specific capacity (301 $mAhg^{-1}$) even after 50 cycles.[8] Furthermore, it exhibits a long and flat voltage plateau at about 0.8 V vs. Li^+/Li, which is much less than that of $Li_4Ti_5O_{12}$ (1.55 V vs. Li^+/Li)[2], offering higher output power. However, PTAL and its derivatives suffer from pretty low electronic conductivity and Li^+ ion diffusion coefficient, which might be the intrinsic problems for most of organic electrode materials.[9,10] As a result, the high rate performance is far from the requirement of the practical application. Very recently, Na^+ ion insertion/extraction behavior of $Na_2C_8H_4O_4$, another representative of terephthalate salt, has been investigated at room temperature, in which the high rate performance still needs further improvement.[11]

There are at least two well-developed methodologies to solve these problems for inorganic electrode materials. One is to reduce particle size down to nanometer scale by sol-gel method, solvothermal synthesis, spray drying, etc.[12] As a consequence, Li^+ ion diffusion distance can be evidently shortened and the specific surface area of the active material can be greatly increased, which will lead to the improvement of the rate capability obviously. The other is to coat conductive material such as Ag[13], amorphous carbon[14], graphite[15], and conductive polymer[1]. The conductive coating layer can form consecutive network, which will enhance electrical conductivity of the composite material. Consequently, the high rate performance can be promoted because of the minimized electrochemical polarization. On the other hand, the assembled architecture of the active material can also play an important role on the electrochemical performance.[16] Porous microsphere consisting of primary nanoparticles is one of the desired hierarchical structures due to its high weight packing density. Furthermore, porous structure can provide 3D mixed conducting network in which widespread micropores allow both

Li^+ ion and electron to migrate rapidly, presenting superior rate performance.

Herein, we have first reported a porous PTAL material with hollow spherical structure synthesized by spray drying method [17]. More importantly, this paper has developed a straightforward surface coating technique for the first time, using solid-state urea as a precursor to deposit a thin N-doped carbon layer on the porous PTAL organic electrode at 400 ºC by chemical vapor deposition (CVD). The porous electrode coated with N-doped carbon reveals unique morphology and excellent electrochemical performance even at room temperature.

Experimental

Preparation of $Li_2C_8H_4O_4$ organic materials

All the experimental chemicals were of analytical grade and used without further purification. The synthesis methodologies were shown in Scheme 1. The bulk PTAL was prepared according to the principle of the acid-base chemical reaction. Terephthalic acid and LiOH were firstly weighted with molar ratio of 1:2, and then the mixture was dispersed in distilled water to form transparent aqueous solution of PTAL organic salt with stirring for 2 h at 80 ºC. Subsequently, the white powder of the bulk PTAL was prepared by evaporating the solution slowly, which was marked as PTALW. Alternatively, the porous PTAL with hollow spherical architecture (named as PTALS) was synthesized by using a common spray drying technology for the PTAL aqueous solution. Following that, PTALS powder and urea reagent, respectively, were transferred into a dual-zone tube furnace and treated at 400 and 200 ºC for x h (x=3, 6 and 9) in Ar atmosphere. Correspondingly, the annealed powder was labelled as PTALSx (x=3, 6 and 9).

Characterization

A Q500 equipment was used for thermogravimetric analysis (TG) with a heating rate of 20 ºC min^{-1} from 50 to 800 ºC in N_2 atmosphere. The crystal structure of the obtained PTAL materials was characterized by X-ray diffraction using Cu Kα radiation (XRD, λ= 1.54056 Å, X'Pert Pro MPD) with a step size of 0.03º in the range of 10 to 50º. Surface morphology was visualized by field-emission scanning electron microscope (FE-SEM, Hitachi, S3400N) and microstructural property was characterized using high-resolution transmission electron microscopy (HRTEM, JEOL, JEM-100CX). The components were analyzed with energy dispersive spectrometer (EDS, Oxford INCA PentaFET-x3) and Fourier Transform Infrared Spectrometer (FT-IR, IRrestige-21) and Raman Spectroscope (Renishaw, inVia Reflex).

Cell assembling and electrochemical test

The electrochemical characterization was carried out by assembling half cells. All PTAL working electrodes were prepared by pasting the slurry onto a clean copper foil. Briefly, the mixed powder consisting of 60 wt.% active material, 30 wt.% carbon black as conducting additive and 10 wt.% polyvinylidene fluoride as the binder was dispersed in N-methyl-2-pyrrolidine (NMP). Finally, the electrode was dried under vacuum at 110 ºC for 12 h. The test cell was assembled in an Ar gas filled glove-box using metallic lithium foil and polypropylene (PP) membrane (Celgard 2400) as the counter electrode and the separator, respectively. 1 mol L^{-1} $LiPF_6$ lucid solution in a 1:1:1 (V:V:V) mixture of ethylene carbonate (EC), diethyl carbonate (DEC) and dimethyl carbonate (DMC) was used as liquid electrolyte.

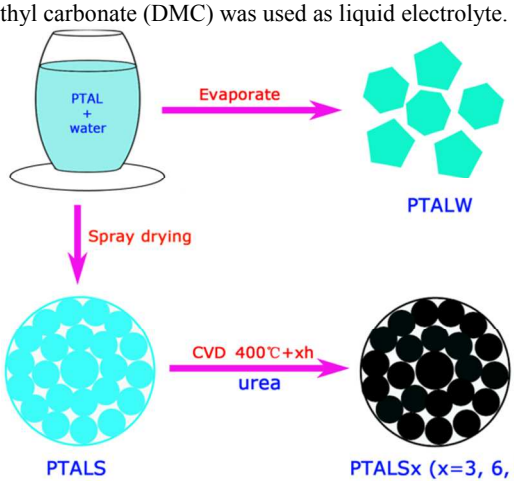

Scheme 1 Schematic of the preparation of the pristine PTALW and PTALS, N-doped C-coated PTALSx (x=3, 6 and 9) materials.

The charge/discharge curves were collected under desired current densities with the voltage between 0.7 and 3.0 V by using a CT2001A cell test instrument (LAND Electronic Co.) at room temperature. Cyclic voltammograms (CV) were performed from 0.5 to 2.5 V at different scanning rates using Solartron SI1287. The electrochemical impedance spectra (EIS) were collected at 0.8 V vs. Li^+/Li in the first discharge process by using an electrochemical workstation (CHI660B) in the frequency range 10^{-2} to 10^5 Hz.

Results and discussion

SEM image of the bulk PATLW indicates the sample is composed of irregularly shaped particles with the maximum size around few ten micrometers (Fig. S1, ESI†). The corresponding XRD profile was matched with the pattern of PTAL pure phase very well (Fig. S2, ESI†).[8] The two strongest peaks are located at 23.2 and 43.4º, respectively, suggesting the preferential crystal growth directions appear along (102) and (112). It is clear that the bulk PTALW consists of well-crystallized PTAL with large grain size.

Fig. 1a displays SEM micrograph of the pristine PTALS sample prepared by spray drying technique. The hollow spheres with the size distribution of 5-10 μm were produced by spray drying technology, which were accumulated by evenly distributed primary nanoparticles with the size of about 500 nm.

The simple heat treatment at 400 °C for 6 h did not change the color of PTALW and PTALS (Fig. S3, ESI†), suggesting there was no obvious surface oxidation or decomposition of PTAL active material occurred. TG measurement confirmed that the decomposition temperature was above 500 °C for both samples (Fig. S4, ESI†). Therefore, it should be safe to set the treating temperature at 400 ºC in the process of carbon coating for $Li_2C_8H_4O_4$ organic salt. Additionally, it should be mentioned that the thermal stability of PTALS was slightly reduced for the nanostructured PTALS since the onset temperature of the carbonization was shifted toward low temperature side, implying the reactive activity of PTALS was enhanced. This might be one

of the limitation factors while considering the columbic efficiency in the first cycle.

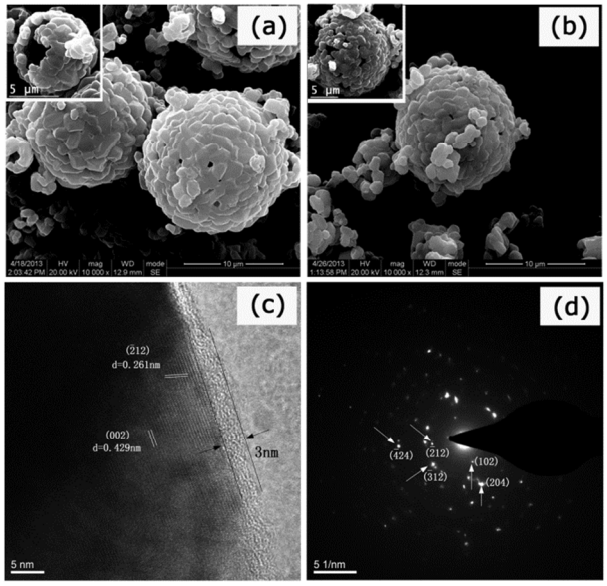

Fig. 1 (a-b) SEM images of the PTALS and PTALS6 sample; (c) HRTEM image of N-doped carbon coated PTALS6 organic material treated by CVD at 400 ºC; (d) SAED pattern of the PTALS6 composite.

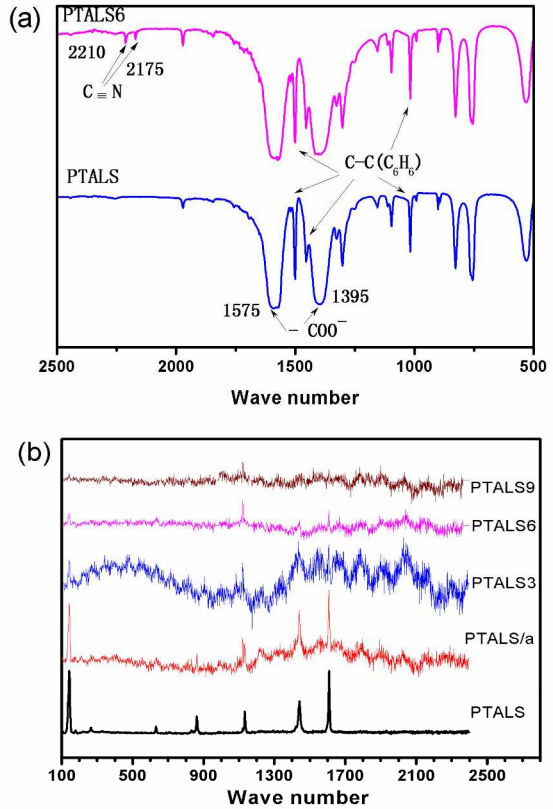

Fig. 2 (a) FT-IR spectra of the pristine PTALS and the carbon coated PTALS6 sample; (b) Raman spectra of the pristine PTALS and as-annealed PTALS (PTALS/a) and the carbon coated samples of PTALSx (x=3, 6 and 9).

While the heat treatment was done in the atmosphere of urea at 400 °C for 3 h, the white color of the pristine PTALS was changed into light gray color. The expanding of the treating period up to 6 h and 9 h can lead to much darker color. The varied color clearly suggests the surface of the porous PTALS has been successfully modified by CVD process. TG curve of PTALS6 illustrates that the thermal stability was enhanced by surface coating since the onset temperature of the carbonization process was elevated (Fig. S4, ESI†). XRD curves of the PTALS and PTALS6 samples are very similar, showing orthorhombic PTAL crystalline phase (Fig. S5, ESI†). Moreover, the coating process did not destroy the morphology of the porous spheres, as indicated by SEM image of the carbon coated PTALS6 sample (Fig. 1b). Hence, it can be easily deduced that the coating layer should be very thin. In order to check the status of the deposited layer, HRTEM and SAED techniques were applied. The corresponding results are demonstrated in Fig. 1c and 1d, separately. HRTEM image shows that the primary particles of the PTALS6 spheres consist of (002) and (212) facets, which is agreement with the XRD result.[8] Furthermore, it can be clearly observed that a uniform and amorphous carbon layer is formed on the surface of each primary particle, where the layer thickness is about 3 nm. The SAED pattern exhibits quite a few discrete points, suggesting the primary particles are well crystallized, and the alignment of the lattice structure is very close to single crystal. Herein, the characteristic lattice distance of the graphitized carbon is not distinguished, which evidences that the coated carbon layer is amorphous.

FT-IR and Raman spectroscopes were further carried out to analyze the composition of the surface coating layer. Fig.2a shows FT-IR spectra of the PTALS before and after coating of 6 h. The coated sample demonstrates two new peaks locating at 2210 and 2175 cm^{-1}, which are ascribed to C≡N stretching modes, respectively.[17,18] Furthermore, the EDS profile of the coating layer shows characteristic X-ray peaks at 0.277, 0.392, and 0.525 KeV (Fig. S6, ESI†), which are allocated to C, N, and O elements, respectively. Taking into account of the dark gray color of the coated samples, it is safely concluded that N element is doped in the carbon layer, where part of N atoms is bonded with C atoms through sp^3 hybridization. This phenomenon is similar to the case of N-doped carbon layer on $Li_4Ti_5O_{12}$.[19] The formation of N-doped carbon coating layer is related with the pyrolysis process of urea. The urea precursor is thermally decomposed into ammonia (NH_3) and isocyanic acid (HNCO) around 160 ºC.[20-21] With the temperature elevated to 400 °C, the intermittent product of HNCO is slowly pyrolyzed to the N-doped carbon compound.

Fig.2b shows Raman spectra of the coated PTALS as a function of the coating time. In order to check the effect of the thermal treatment at 400 °C, the spectrum of the as-annealed PTALS for 6 h was also provided. The Raman spectra superimpose for the pristine and as-annealed samples, again confirming that the simple thermal treatment does not destroy molecular structures greatly. After coating for 3h, the characteristic peaks of PTAL become weak. While the coating time was further increased to 9 h, the spectrum of the PTALS9 was almost featureless. Since Raman signal is very sensitive to surface species, the reduced signal intensity indicates that the coating layer thickness is increased with the deposition time.

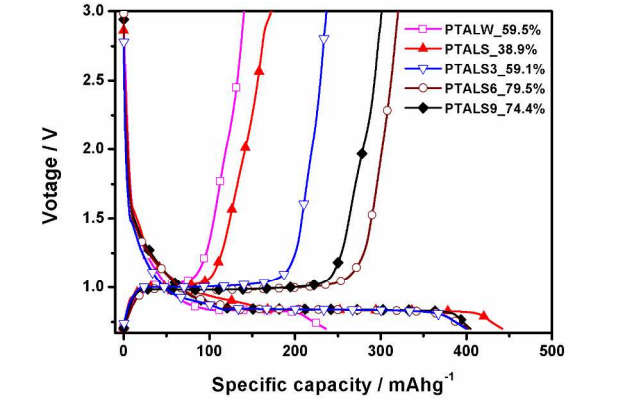

Fig. 3 The first discharge/charge profiles of the PTALW, PTALS and carbon coated PTALSx (x=3, 6 and 9).

Fig. 3 displays the first discharge/charge profiles of the bulk PTALW, porous PTALS and N-doped carbon-coated PTALSx (x=3, 6 and 9) materials at a rather low rate of 0.05 C. A flat discharge voltage plateau at 0.83 V was observed for all the pure and coated samples, reflecting the typical Li^+ ion insertion process of PTAL.[8] The PTALW discharge capacity is only 236 mAh g^{-1}, which might be related with the relatively large particle size. While the feature size of the active material was shrunken, the first discharge capacity was greatly increased to 442, 400, 403 and 405 mAh g^{-1}, for porous PTALS, and coated PTALSx (x=3, 6 and 9) samples, respectively. It is apparent that the nanosized electroactive material with large surface area can aid for further utilization of the potential capacity of the active material.

The coulombic efficiency in the first cycle is one of the important indicators to evaluate electrochemical performance of the desired electrode materials. Here, the bulk PTALW shows relatively low efficiency of 59.5% in the first cycle. However, the coulombic efficiency of the PTALS electrode is only 38.9%, even lower than that of the bulk PTALW. One of the possible reasons is related with the formation of solid electrolyte interface (SEI) passivating film on the surface, which might occur above 0.8 V in the first discharge process. Porous PTALS offers large specific surface area, which will lead to large irreversible capacity. As a consequence, the efficiency became bad despite that both discharge and charge capacities were increased for PTALS. After surface modification of the organic anode material at 400 °C for 3, 6, and 9 h, the initial efficiencies respectively were enhanced to 59.1%, 79.5% and 74.4%. Since the morphology of the pristine PTALS and the coated PTALSx (x=3, 6 and 9) compounds is not obviously modified, it is reasonable to assume that the surface area is not changed greatly, which is proved by the fact that all of the three coated samples have nearly the same discharge capacity in the first cycle. The difference of the columbic efficiencies in the first cycle is determined by the charge process. PTALS6 shows the largest charge capacity. It was reported that the coating layer with moderate thickness can keep the best balance point between the electronic conductivity and ionic conductivity, resulting in the best electrochemical performance.[19] The rule should be applied to PTALS6, where the medium coating layer thickness provides the maximum delithiation degree and the best coulombic efficiency.

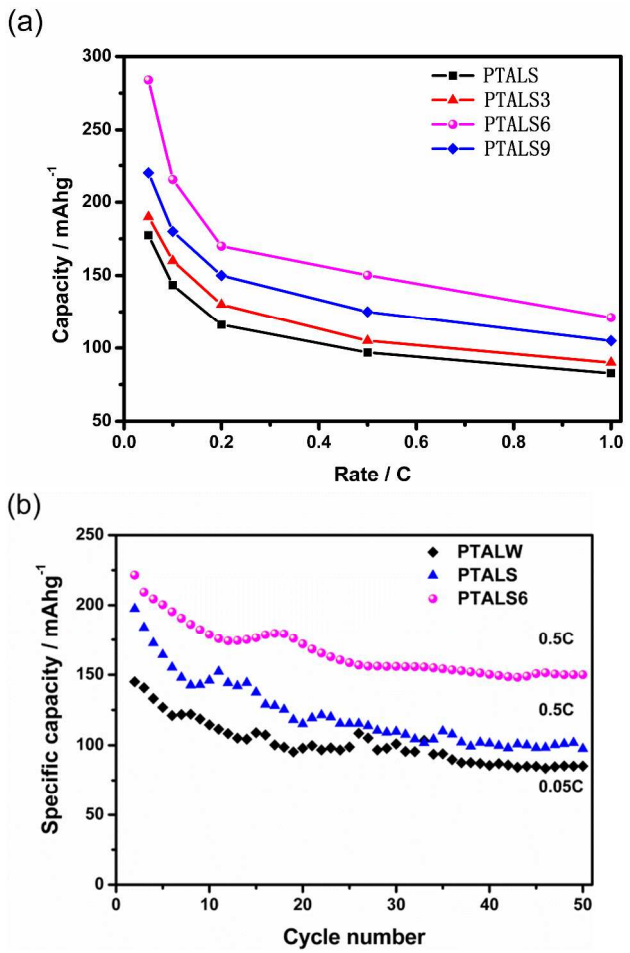

Fig. 4 (a) Specific capacities of the pristine PTALS sample and PTALSx (x=3, 6 and 9) with an uniform carbon layer at different current rates; (b) The cycling performance of the bulk PTALW, porous PTALS and coated PTALS6.

The coated PTALSx (x=3, 6 and 9) samples were further tested to cycle at different charge/discharge current densities. As a reference, the rate capability of the white pristine PTALS sample was provided, too. Fig. 4a reveals the typical discharge capacities of the pristine PTALS and coated PTALSx (x=3, 6 and 9) electrode materials as a function of current rate. It is clear that the reversible capacities of the coated samples are always larger than that of the unmodified PTALS at the same current rate, and PTALS6 provides the best electrochemical performance at any current density. The representative voltage curves of the PTALS and PTALS6 under the discharge current rate of 0.05, 0.1, 0.2, 0.5, and 1 C are shown in Fig. S7 (ESI†). At the lowest rate of 0.05 C, PTALS6 gives the highest discharge capacity of 259 mAh g^{-1} at the second cycle. With the current rate increasing from 0.1, 0.2, 0.5 and 1 C, the specific discharge capacity is slowly down to 215, 170, 150 and 121 mAh g^{-1}, respectively.

Fig. 4b shows the cycling performance of the bulk PTALW, porous PTALS and coated PTALS6 from the second cycle. The bulk PTALW was tested at the lowest current rate of 0.05C, where the discharge capacity was only about 145 mAh g^{-1} at the second cycle, and remained at 85 mAh g^{-1} after 50 cycles, with low capacity retention of 58.6%. Even the current density was enlarged by ten times, the porous PTALS still exhibited specific

capacity of 98 mAhg^{-1} at the 50th cycle, implying the reduced feature size does not break the structural integrity and chemical/electrochemical stability of the active material. After further coating with N-doped carbon layer, the discharge capacity was further promoted to 221 mAhg^{-1} at the second cycle, which slowly decayed to 150 mAh g^{-1} at the 50th cycle, keeping capacity retention of 67.9%. This result demonstrates that the nanostructured electrode and the surface coating can effectively improve the cycling performance of the organic electrode.

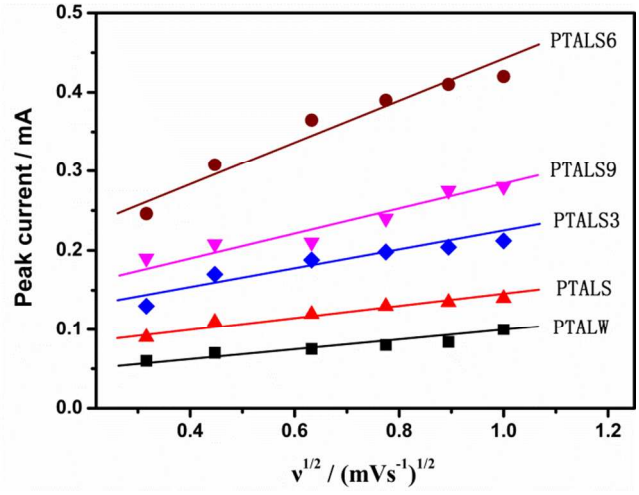

Fig. 5 Peak current against square root of scan rate for the pure PTALW, PTALS and carbon modified PTALSx (x=3, 6 and 9) samples.

In order to gain a deep insight on the electrochemical reaction mechanism during Li^+ ion insertion/extraction process and the influence of the coating layer on the kinetic performance, CV curves with a potential window of 0.5 to 2.5 V *vs.* Li^+/Li were recorded for the bulk PTALW, porous PTALS and the coated PTALSx. Compared to the bulk PTALW, porous PTALS and PTALSx (x=3, 6 and 9) samples with hollow spherical morphology display higher peak currents at the same scan rate (Fig. S8, ESI†). The relationship between the peak currents and square roots of different scan rates was depicted in Fig. 5. All of the data for each of the samples can be fitted with a straight line, which is the typical behavior of diffusion-controlled reaction.[22] Li^+ ion diffusion coefficient of the specific electrode material is proportional to the slope of each inclined line. The slope of PTALS is only slightly larger than that of PTALW, suggesting the diffusion coefficient is not greatly improved. It can be easily interpreted that the reduced particle size does not influence Li^+ ion diffusion process greatly since the highly crystallized two materials have nearly defect-free structure. Very interestingly, the lines of the PTALSx (x=3, 6 and 9) samples are steeper than that of the pristine PTALS. Hence it can be deduced that the apparent diffusion coefficient of the coated electrodes is larger than that of the pure material, which should benefit for better performance under high current density. The PTALS6 with medium coating layer thickness shows the maximum diffusion coefficient. However, this tendency is contrast to the carbon coated $Li_4Ti_5O_{12}$, where the coating layer always impedes Li^+ ion diffusion regardless of the layer thickness.[19b] Herein, the magical phenomenon is supposed to be correlated with the change of the surface physical/chemical condition in the process of the coating, which makes a favor of Li^+ transferring and transporting. The detailed reason is under further investigation.

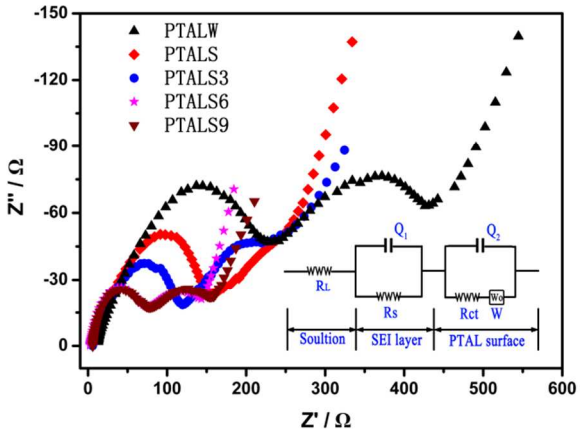

Fig. 6 EIS of the pristine PTALS white powders and the carbon coated PTALSx (x=3, 6 and 9).

	Rl	Rs	CPE1	Freq1	Rct	Warbug	CPE2	Freq2
PTALW	11.5	177	2.1E-5	0.74	211	0.021	1.3E-3	0.73
PTALS	4.6	152	1.1E-5	0.76	147	0.021	4.5E-3	0.50
PTALS3	4.3	118	3.3E-3	0.76	120	0.034	3.4E-2	0.71
PTALS6	4.0	68	6E-5	0.79	70	0.085	5.0E-3	0.65
PTALS9	4.1	70	7E-5	0.68	75	0.056	3.2E-3	0.69

Fig. 6 shows EIS plots of all of the organic electrode materials. These plots are quite similar in shape, consisting of two semicircles and an inclined line. The semicircle in high frequency range was attributed to SEI passivating film, and the other semicircle represents the charge transfer process for high-middle frequencies.[23-25] An equivalent circuit was used to fit these impedance spectra by Zview software (Fig. 6, inset). Here R_l, R_s and R_{ct} represent ionic resistance of the electrolyte, passivating film resistance, and charge transfer resistance, respectively. Q1 and Q2 represent CPE constant phase elements. Table 1 displays these parameters obtained by fitting. The bulk PTALW exhibits the largest film resistance of 177 Ω, which becomes small for the PTALS. The coating process makes the resistance down to 118, 68, 70 Ω for PTALS3, PTALS6, PTALS9, separately. On the other hand, the charge transfer resistance R_{ct} of PTALS is 152 Ω, which is lower than that of PTALW (ca. 211 Ω). The resistance is further reduced by coating, and the lowest value is 70 Ω for PTALS6. These results indicate the porous structure and coating technique could benefit for perfecting the passivated film and accelerate the charge transfer reaction. Briefly, the PTALS6 featured with the moderate thickness of the electronic conductive coating layer has the maximum apparent Li^+ ion diffusion coefficient, leading to the lowest passivating layer resistance and charge transfer resistance, which undoubtly yields the highest columbic efficiency in the first cycle and the largest delithiation capacity as well as the best cycling performance.

Conclusions

In conclusion, we have succeeded in developing a straightforward hybrid methodology to prepare microsphere PTAL-based organic anode materials with a uniform N-doped carbon amorphous layer for advanced electrochemical

performance, where each hollow sphere was assembled with evenly distributed PTAL nanocrystals. The coulombic efficiency in the first cycle was quickly elevated up to 79.5% by the coating technique in contrast with the pristine porous PTALS sample of 38.9%, which was assigned to the formation of qualified SEI film in the first discharge process. Moreover, the coating layer can greatly promote the high rate performance as well as the cycling performance. PTALS6 shows the largest reversible capacity of 150 mAh g^{-1} at 0.5 C after 50 cycles, which is much larger than 85 mAh g^{-1} even at 0.05 C for the bulk PTALW. The simply combination of the spray drying method and CVD coating technique is a unique route to fabricate organic anode composite material for excellent electrochemical performance. Our findings might trigger the interest to study organic electrode materials featured with good solubility and low electronic conductivity for potential application in low-cost battery and large-scale energy storage.

Acknowledgements

This work was supported by funding from NSFC (nos. 21073029, 11234013, 51211140045), RFDP (no. 20100185110019), Program for New Century Excellent Talents in University (no. NCET-10-0296), the Fundamental Research Funds for the Central Universities (no. ZYGX2012Z003).

Notes and references

State Key Laboratory of Electronic Thin Films and Integrated Devices, School of Microelectronics and Solid-state Electronics, University of Electronic Science and Technology of China, Chengdu, China. Fax: +86 28 83202569; Tel: +86 28 83207620; E-mail: lijingze@uestc.edu.cn

† Electronic Supplementary Information (ESI) available: See DOI: 10.1039/b000000x/

1 L. W. Ji, Z. Lin, M. Alcoutlabi and X. W. Zhang, *Energy Environ. Sci.*, 2011, **4**, 2682; C. Liu, F. Li, L. P. Ma and H. M. Cheng, *Adv. Mater.*, 2010, **22**, E28.

2 J. Chen, L. N. Xu, W. Y. Li and X. L. Gou, *Adv. Mater.*, 2005, **17**, 582; P. Poizot, S. Laruelle, S. Grugeon, L. Dupont and J. -M. Tarascon, *Nature*, 2000, **407**, 496; B. Varghese, M. Reddy, Z. Yanwu, C. S. Lit, T. C. Hoong, G. Subba Rao, B. Chowdari, A. T. S. Wee, C. T. Lim and C. H. Sow, *Chem. Mat.*, 2008, **20**, 3360; J. Z. Li, H. Li, Z. X. Wang, X. J. Huang and L. Q. Chen, *J. Power Sources*, 1999, **81-82**, 346.

3 A. L. M. Reddy, A. Srivastava, S. R. Gowda, H. Gullapalli, M. Dubey and P. M. Ajayan, *Acs Nano*, 2010, **4**, 6337.

4 C. X. Bao, H. Huang, J. Yang, H. Gao, T. Yu, J. G. Liu, Y. Zhou, Z. S. Li and Z. G. Zou, *Nanoscale*, 2013, **5**, 4951.

5 J. K. Lee, K. B. Smith, C. M. Hayner and H. H. Kung, *Chem. Commun.*, 2010, **46**, 2025; J. W. Li, A. J. Zhou, X. Q. Liu and J. Z. Li, *J. Inorg. Mater.*, 2013, **28**, 1207.

6 J. Z. Chen, L. Yang, S. H. Fang, S. Hirano and K. Tachibana, *J. Power Sources*, 2012, **200**, 59.

7 Y. L. Liang, Z. L. Tao and J. Chen, *Adv. Energy Mater.*, 2012, **2**, 742; Z.P. Song and H. S. Zhuo, *Energy Environ. Sci.*, 2013, **6**, 2280; M. Armand and J. -M. Tarascon, *Nature*, 2008, **451**, 652.

8 M. Armand, S. Grugeon, H. Vezin, S. Laruelle, P. Ribiere, P. Poizot and J. M. Tarascon, *Nat. Mater.*, 2009, **8**, 120; J. A. Kaduk, *Acta Crystallogr., Sect. B: Struct. Sci.*, 2000, **56**, 474; Y. Y. Zhang, Y. Y. Sun, S. X. Du, H. J. Gao and S. B. Zhang, *Appl. Phys. Lett.*, 2012, **100**, 091905.

9 J. Chen, S. Wang, L. Wang, K. Zhang, Z. Zhu and Z. Tao, *Nano Lett.*, 2013, **13**, 4404; W. Walker, S. Grugeon, O. Mentre, S. Laruelle, J.-M. Tarascon and F. Wudl, *J. Am. Chem. Soc.*, 2010, **132**, 6517.

10 H. X. Zhang, D. L. Li, L. Gou, X. Y. Fan and Q. Li, *Chin. J. Power Sources*, 2012, **36**, 470.

11 L. Zhao, J. M. Zhao, Y. S. Hu, H. Li, Z. B. Zhou, M. Armand and L. Q. Chen, *Adv. Energy Mater.*, 2012, **2**, 962; Y. Park, D. S. Shin, S. H. Woo, N. S. Choi, K. H. Shin, S. M. Oh, K. T. Lee and S. Y. Hong, *Adv. Mater.*, 2012, **24**, 3562; A. Abouimrane, W. Went, H. Eltayeb, Y. Cui, J. Niklas, O. Poluektov and K. Amine, *Energy Environ. Sci.*, 2012, **5,** 9632.

12 D. Yoshikawa, Y. Kadoma, J. M. Kim, K. Ui, N. Kumagai, N. Kitamura and Y. Idemoto, *Electrochim. Acta*, 2010, **55**, 1872; S. H. Yu, A. Pucci, T. Herntrich, M. G. Willinger, S. H. Baek, Y. E. Sung and N. Pinna, *J. Mater. Chem.*, 2011, **21**, 806.

13 B. L. He, B. Dong and H. L. Li, *Electrochem. Commun.*, 2007, **9**, 425.

14 M. Yoshio, H. Wang, K. Fukuda, T. Umeno, N. Dimov and Z. Ogumi, *J. Electrochem. Soc.*, 2002, **149**, A1598.

15 H. G. Jung, J. Kim, B. Scrosati and Y. K. Sun, *J. Power Sources*, 2011, **196**, 7763.

16 J. Hu, M. Chen, X. S. Fang and L. Wu, *Chem. Soc. Rev.*, 2011, **40**, 5472.

17 N. Tran, K. Bramnik, H. Hibst, J. Prolß, N. Mronga, M. Holzapfel, W. Scheifele and P. Novak, *J. Electrochem. Soc.*, 2008, **155**, A384; Z. Y. Wen, Z. H. Gu, S. H. Huang, J. H. Yang, Z. X. Lin and O. Yamamoto, *J. Power Sources*, 2005, **146**, 670.

18 Q. X. Guo, Y. Xie, X. J. Wang, S. Y. Zhang, T. Hou and S. C. Lv, *Chem. Commun.*, 2004, **1**, 26; Q. Lv, C. B. Cao, C. Li, J. T. Zhang, H. X. Zhu, X. Kong and X. F. Duan, *J. Mate. Chem.*, 2003, **13**, 1241.

19 L. Zhao, Y. S. Hu, H. Li, Z. X. Wang and L. Q. Chen, *Adv. Mater.*, 2011, **23**, 1385; H. Q. Zhang, Q. J. Deng, C. X. Mou, Z. L. Huang, Y. Wang, A. J. Zhou and J. Z. Li, *J. Power Sources*, 2013, **239**, 538; H. Niwa, K. Horiba, Y. Harada, M. Oshima, T. Ikeda, K. Terakura, J.-i. Ozaki and S. Miyata, *J. Power Sources*, 2009, **187**, 93.

20 S. D. Yim, S. J. Kim, J. H. Baik, I. S. Nam, Y. S. Mok., J. H. Lee, B. K. Cho and S. H. Oh, *Ind. Eng. Chem. Res.*, 2004, **43**, 4856.

21 H. L. Pan, L. Zhao, Y. S. Hu, H. Li and L. Q. Chen, *Chemsuschem*, 2012, **5**, 526.

22 N. Schweikert, H. Hahn and S. Indris, *Phys. Chem. Chem. Phys.*, 2011, **13**, 6234.

23 Y. D. Ko, J. G. Kang, J. G. Park and D. W. Kim, *J. Appl. Electrochem.*, 2010, **40**, 109.

24 H. Li, X. J. Huang and L. Q. Chen, *J. Power Sources*, 1999, **81**, 340.

25 S. S. Zhang, K. Xu and T. R. Jow, *Electrochim. Acta*, 2006, **51**, 1636.